Contrib Mineral Petrol (2007) 154:15–34
DOI 10.1007/s00410-006-0177-1

ORIGINAL PAPER

Water partitioning between mantle minerals from peridotite xenoliths

Kevin Grant · Jannick Ingrin · Jean Pierre Lorand · Paul Dumas

Received: 6 April 2006 / Accepted: 21 December 2006 / Published online: 5 April 2007

Abstract The speciation and amount of water dissolved in nominally anhydrous silicates comprising eight different mantle xenoliths has been quantified using synchrotron micro-FTIR spectroscopy. Samples studied are from six geographic localities and represent a cross-section of the major upper mantle lithologies from a variety of tectonic settings. Clinopyroxene contains between 342 and 413 ppm H_2O. Orthopyroxene, olivine and garnet contain 169–201, 3–54 and 0 to <3 ppm H_2O, respectively. Pyroxenes water contents and the distribution of water between ortho- and clinopyroxene is identical regardless of sample mineralogy ($D_{water}^{cpx/opx}$ = 2.1 ± 0.1). The total water contents of each xenolith are remarkably similar (113 ± 14 ppm H_2O). High-resolution spectroscopic traverses show that the concentration and speciation of hydrous defects dissolved in each phase are spatially homogeneous within individual crystals and identical in different crystals interspersed throughout the xenolith. These results suggest that the amount of water dissolved in the silicate phases is in partial equilibrium with the transporting melt. Other features indicate that xenoliths have also preserved OH signatures of equilibrium with the mantle source region: Hydroxyl stretching modes in clinopyroxene show that garnet lherzolites re-equilibrated under more reducing conditions than spinel lherzolites. The distribution of water between pyroxenes and olivine differs according to xenolith mineralogy. The distribution of water between clinopyroxene and olivine from garnet peridotites ($D_{water}^{cpx/oliv}$(gnt) = 22.2 ± 24.1) is a factor of four greater than mineral pairs from spinel-bearing xenoliths ($D_{water}^{cpx/oliv}$(sp) = 88.1 ± 47.8). Such an increase in olivine water contents at the spinel to garnet transition is likely a global phenomenon and this discontinuity could lead to a reduction of the upper mantle viscosity by 0.2–0.7 log units and a reduction of its electrical resistivity by a factor of 0.5–0.8 log units.

Keywords Hydrogen · Water · Mantle xenoliths · Partition coefficients · Garnet lherzolites · Conductivity · Viscosity · Lithospheric mantle

Communicated by M.W. Schmidt.

K. Grant
ARC Key Centre for the Geochemistry and Metallogeny of the Continents (GEMOC), Department of Earth and Planetary Sciences, Macquarie University, Sydney, NSW, Australia

J. Ingrin (✉)
LMTG, Université de Toulouse, CNRS, IRD, OMP, Avenue Edouard Belin, 31400 Toulouse, France
e-mail: ingrin@lmtg.obs-mip.fr

J. P. Lorand
Unité Scientifique du Muséum « Minéralogie – Pétrologie » CNRS UMR 7160, Muséum National d'histoire Naturelle, 61 rue Buffon, 75005 Paris, France

P. Dumas
Synchrotron SOLEIL, l'Orme des Merisiers, St Aubin BP 48, 91192 Gif sur Yvette, France

Introduction

Mantle-derived peridotite xenoliths, which are classified according to the relative proportions of the three main phases: olivine, orthopyroxene and clinopyroxene, and an additional pressure-dependant, aluminous phase, offer a unique opportunity to directly sample the composition of the sub-continental lithosphere. Although nominally anhydrous, hydrogen is commonly found in natural samples of each of these phases (except for aluminous spinel:

A. Beran, personal communication) where upon bonding with oxygen atoms in the silicate structure it forms hydroxyl groups. However, because hydrogen diffuses extremely rapidly through the crystal structure of nominally anhydrous phases (see Ingrin and Blanchard 2006 and references therein) the water contents of mantle-derived nominally anhydrous phases could re-equilibrate following entrainment in the host magma. Indeed, two recent studies have interpreted spatially zoned water concentrations in mantle-derived olivine as direct evidence of dehydration during ascent (Demouchy et al. 2006; Peslier and Luhr 2006). As trace amounts of water dissolved in nominally anhydrous phases will profoundly influence the strength, elastic properties and melting temperatures of rocks, minerals and melts (Hirth and Kohlstedt 1996; Karato 1990; Mackwell et al. 1985), accurately quantifying the amount of water at depth is of critical importance. It would be extremely useful to understand from where the water dissolved in mantle xenoliths is derived and what information the hydrogen contents of a xenolith can tell us about processes in the deep Earth.

Infrared micro-spectroscopy (μ-FTIR) is commonly employed to measure trace amounts of water in nominally anhydrous phases. The technique suffers limitations in domain size analysis, since the typical black body IR source does not provide sufficient flux to achieve diffraction-limited spatial resolution of the technique. Synchrotron sourced infrared micro-spectroscopic studies employ a source that is 100–1,000 times brighter than when traditional black body source is used, therefore offering significantly enhanced spatial resolution compared to traditional methods (Dumas and Miller 2003).

Controversy over the origin and geological significance of water defects dissolved in the silicate phases comprising mantle xenoliths can be directly attributed to a lack of understanding as to the processes responsible for generating the observed concentrations. The purpose of this study was to investigate the processes responsible for the observed signatures by quantifying water species dissolved in coexisting clinopyroxene, orthopyroxene, olivine, spinel and garnet crystals found in well characterised, natural xenoliths using synchrotron and polarized μ-FTIR spectroscopy. Our aims were to, (1) use high-resolution synchrotron μ-FTIR to measure the concentration and speciation of hydrous species dissolved in natural samples of the dominant upper mantle silicates, (2) quantify water contents as a function of distance from the rim in individual crystals, (3) explore how hydrogen partitions between different phases, (4) correlate water solubility data with the provenance of the xenolith and (5) investigate the relative merits of synchrotron and polarized black-body μ-FTIR spectroscopy as tools for analysing geological samples. Our results allow us to place constraints on the evolution of xenolith water contents during their ascent from the source region, understand the relevance of dissolved water contents with regard to interpreting those anticipated at depth, compare the hydrogen contents of nominally anhydrous minerals estimated using two spectroscopic methods and, evaluate the water content of the upper mantle and how this may influence its physical properties.

Samples

Eight mantle xenoliths were chosen for this study (Table 1). Four were hosted in alkali basalts (BAR8303, KHL8302, KHL8306, KHL8308) and four from kimberlitic magmas (B13, KJB30 LMA15, LTP15). Samples were chosen to represent the lithospheric upper mantle from various depths and under a variety of tectonic settings. Three spinel lherzolites (KHL8302, KHL8306, KHL8308) are from Kilbourne Hole, New Mexico, and another (BAR8303) from the volcanic centre of Barges (Massif

Table 1 Provenance, paragenesis and type of the peridotite xenoliths analysed in this study

Sample	Rock type	Locality	Mineral assemblage	*P* (GPa)	*T* (°C)
BAR8303	Sp peridot.	Barges	Ol[54] + opx[34] + cpx[11] + sp[1]	1.25	927
KHL8302	Sp peridot.	Kilbourne Hole	Ol[51] + opx[31] + cpx[16] + sp[2]	1.12	932
KHL8306	Sp peridot.	Kilbourne Hole	Ol[54] + opx[29] + cpx[13] + sp[4]	1.74	1,034
KHL8308	Sp peridot.	Kilbourne Hole	Ol[60] + opx[25] + cpx[14] + sp[1]	2.76	1,171
B13	Gnt peridot.	Bultfontein	Ol[64] + opx[31] + gnt[5] + trace cpx	4.56	974
KBJ30	Gnt peridot.	Jagersfontein	Ol[55] + opx[38] + gnt[3] + cpx[4]	5.7–7.0	1,201–1,326
LMA15	Gnt peridot.	Matsuko	Ol[41] + opx[53] + gnt[1] + cpx[5]	3.7–5.1	916–1,090
LTP15	Gnt peridot.	Thaba Putsoa	Ol[61] + opx[25] + gnt[2] + cpx[12]	6.5–7.4	1,380–1,518

Numbers in square brackets are estimated modal proportions of each phase. Pressure and temperature conditions were estimated using geothermometers and geobarometers (Bertrand and Mercier 1985; Brey and Köhler 1990; Nimis and Taylor 2000)

Mineral abbreviations: *ol* olivine, *opx* Orthopyroxene, *cpx* clinopyroxene, *sp* spinel, *gnt* garnet

Central, France). Kimberlite-hosted xenoliths come from the petrological collection of the Natural History Museum (Paris). They were from two well-known South African kimberlite pipes (Jagersfontein, Bultfontein; KJB30, B13) and other two famous localities in Northern Lesotho (Matsoku, Thaba Putsoa; LMA15, LTP15).

Sample petrology

Spinel-bearing samples

The four spinel lherzolites (BAR8303, KHL8302, KHL8306 and KHL8308) are coarse-grained and exhibit well-equilibrated, equigranular structures. The 120° triple junctions are common between the subhedral olivine and orthopyroxene grains, which normally exceed 2 mm in diameter. Clinopyroxene and spinel are much smaller (0.5–1 mm in diameter) and more irregular shaped. Polished sections of individual crystals of each phase in the spinel lherzolites are optically transparent. Fractures and inclusions were rare and crystal interfaces between any two grains are exceptionally well defined. No evidence of additional phases, melt or alteration associated with modal metasomatism or any form of alteration was observed.

Constituent phase chemistries (Table 2) were obtained using the Cameca SX50 electron microprobe at the Uni-

Table 2 Representative compositions of minerals (average values)

	BAR8303				KHL8302				KHL8306				KHL8308			
	cpx	opx	oliv	spin	cpx	opx	oliv	spin	cpx	opx	oliv	spin	cpx	opx	oliv	spin
SiO_2	51.37	55.94	41.02	0.05	52.13	54.82	40.65	0.31	51.2	54.82	40.7	0.07	52.48	54.5	40.96	0.09
TiO_2	0.48	0.09	0.01	0.12	0.6	0.1	0.02	0.11	0.05	0.09	0	0.01	0.29	0.12	0.03	0.16
Al_2O_3	6.55	3.82	0.02	53.44	7.44	4.98	0	58.37	5.11	4.98	0	45.02	6.82	5.26	0.04	49.15
Cr_2O_3	0.9	0.29	0	13.28	0.78	0.34	0	9.34	1.21	0.34	0.03	22.32	1.27	0.69	0.04	17.51
FeO[a]	2.79	6.17	9.22	9.13	2.85	6.03	9.7	8.91	2.68	6.03	8.09	8.16	3.14	5.54	8.53	7.86
MnO	0.06	0.02	0.11	0.05	0.03	0.17	0.12	0.08	0.07	0.17	0.13	0.13	0.09	0.12	0.18	0.12
NiO	0.01	0.08	0.39	0	0.03	0.12	0.4	0.37	0	0.12	0.36	0.29	0.06	0.12	0.32	0.28
MgO	15.4	33.31	49.06	20.15	14.99	32.16	48.88	20.82	16.11	32.16	49.62	20.12	16.81	31.73	48.96	20.48
CaO	20.53	0.63	0.09	0	20.11	0.73	0.07	0	19.55	0.73	0.09	0	18.23	1.42	0.19	0.01
Na_2O	1.79	0.09	0.02	0.01	1.85	0.09	0.01	0	4.75	0.39	0.02	0	1.35	0.15	0	0
K_2O	0	0	0	0	0	0	0	0	0	0	0	0	0	0.15	0	0
Fe_2O_3	–	–	–	2.56	–	–	–	1.45	–	–	–	3.88	–	–	–	3.07
Sum	99.88	100.44	99.96	98.79	100.81	99.54	99.48	99.76	100.74	99.83	99.04	100	100.56	99.8	99.25	98.73
XMg[b]	0.908	0.905	0.9	0.79	0.904	0.904	0.89	0.8	0.912	0.904	0.91	0.84	0.905	0.91	0.91	0.82

	B13			KBJ30				LMA15				LTP15			
	opx	oliv	gnt	cpx	opx	oliv	gnt	cpx	opx	oliv	gnt	cpx	opx	oliv	gnt
SiO_2	58.06	42.36	42.20	54.70	57.03	40.39	43.73	54.59	58.68	41.56	42.12	55.90	57.97	41.98	42.74
TiO_2	0.01	0	0.02	0.44	0.22	0.10	0.73	0.06	0.01	0.01	0.02	0.17	0.10	0	0.49
Al_2O_3	0.66	0	19.98	2.70	0.89	0	21.69	2.94	0.67	0	19.34	1.83	0.95	0	20.51
Cr_2O_3	0.35	0	4.97	0.66	0.14	0	1.63	2.42	0.38	0.04	5.93	0.85	0.34	0.05	3.32
FeO[a]	3.49	5.75	5.83	3.15	6.01	10.23	7.87	2.38	4.13	7.43	5.92	3.27	4.56	7.63	6.01
MnO	0.09	0.09	0.32	0.12	0.10	0	0.24	0.14	0.15	0	0.30	0.06	0.12	0.05	0.21
NiO	ND	0.36	ND	ND	0.14	0.21	ND	ND	ND	0.43	ND	ND	ND	0.25	ND
MgO	35.09	50.83	19.95	17.39	33.94	48.61	20.65	15.67	35.23	49.10	19.62	20.09	33.73	49.57	20.97
CaO	0.36	0.04	5.54	17.00	0.87	0	4.43	18.21	0.47	0.10	5.85	16.40	1.50	0.11	4.94
Na_2O	0	0	–	2.05	0.19	0.05	–	2.76	0	–	–	1.11	0.02	–	–
K_2O	0.01	0	–	0.01	0	0	–	0.04	0.03	–	–	0.05	0.01	–	–
Sum	98.12	99.44	98.81	98.23	99.55	99.61	100.9	99.21	99.75	98.68	99.11	99.72	99.30	99.64	99.19
XMg[b]	0.950	0.940	0.859	0.908	0.909	0.890	0.824	0.965	0.930	0.920	0.855	0.916	0.920	0.920	0.861

cpx Clinopyroxene, *opx* Orthopyroxene, *oliv* olivine, *gnt* garnet, spin spinel

[a] Except for spinel, all Fe reported as FeO

[b] $X^{Mg} = Mg/(Mg + Fe^{2+})$

versity Paul Sabatier, Toulouse. An accelerating voltage of 15 kV and a beam current of 15 nA were used to all analyses. Clinopyroxene are diopsides (En48.3–53.1; Fs4.9–5.6; Wo41.4–46.5), orthopyroxene are Al rich (Al_2O_3 = 3.82–5.26 wt%) and $X_{Mg}^{olivine}$ is always lower than 0.91. X_{Mg}^{spinel} ranges between 0.79 and 0.84 and X_{Cr}^{spinel} [X_{Cr}^{spinel} = Cr/(Cr + Al)] vary between 0.09 and 0.25. No chemical zoning was observed in any of the crystals analysed.

Equilibration conditions of the spinel lherzolite samples were calculated using the Ca-in-olivine geothermobarometer (Bertrand and Mercier 1985). Spinel lherzolite xenoliths re-equilibrated at T = 927–1,171°C and at estimated pressures corresponding to depths ranging between 30 and 80 km (Table 1).

Garnet-bearing samples

The modal proportion of clinopyroxene in the garnet-bearing samples ranges from <1 to 12%. Garnet compositions plot in the lherzolite field of the CaO versus Cr_2O_3 plot of Sobolev et al. (1973). None of the garnet-bearing xenoliths show any textural evidence of deformation. KBJ30 (Jagersfontein) comprises large, subhedral orthopyroxene, clinopyroxene and garnet (crystals 1–3 mm in diameter) surrounded by finer-grained euhedral olivine crystals (0.5 mm in diameter). LTP15 (Thaba Putsoa) and LMA15 (Matsoku) are both equigranular (average crystal diameters of 1–3 mm and 2–5 mm in LTP15 and LMA15, respectively). In all of the garnet-bearing samples, garnet occurs as rounded crystals, which in some cases are fractured and surrounded by a thin kelyphite rim. In addition, fine-grained, brown alteration products are frequently observed along phase boundaries, in cracks or fractures and as inclusions in many phases comprising the garnet lherzolite xenoliths. These are discussed in more detail later.

Garnets in samples B13 (Bultfontein), LMA15 and LTP15 are purple. Those from KBJ30 are bright rose-red. Clinopyroxene are bright green in all samples and mostly occurs in close spatial association with garnet crystals. B13 is coarse grained and dominated by olivine, orthopyroxene, and garnet with very minor clinopyroxene (<1% mode). Individual crystals measure 2–4 mm in diameter although occasional olivine grains up to 6 mm in diameter are also found. Purple garnet crystals normally measure 1.5–2 mm, but occasionally up to 3 mm in diameter. Grain boundaries between olivine, orthopyroxene and garnet are mostly smoothly curved.

Clinopyroxenes from garnet lherzolite xenoliths contain lower amounts of aluminium and are slightly richer in magnesium (En53.4–59.9; Fs1.9–4.9; Wo35.2–44.6) than those from spinel lherzolites. X_{Mg}^{cpx} (=Mg/[Mg + Fe]) varies between 0.90 and 0.96. Orthopyroxene are poorer in Al (Al_2O_3 = 0.66–0.95 wt%) than those from spinel lherzolites. $X_{Mg}^{olivine}$ ranges from 0.89 to 0.94, including refractory and more fertile xenoliths (KBJ30). The garnets are all Cr-pyropes (Cr_2O_3 > 1 wt%) although they may also show significant almandine (Alm 11–15.5) grossular (Gr 0–6.5), and uvarovite (Uv 4.7–17) components. X_{Mg}^{garnet} are all >0.65 indicating that they are in equilibrium with mantle olivine (Griffin et al. 1999). No chemical zoning was observed in any of the crystals analysed.

Equilibration P–T conditions of the garnet-bearing samples were estimated using the two-pyroxene geothermometer, Ca-in-orthopyroxene geothermometer, and the coupled Cr-in-clinopyroxene geobarometer and enstatite-in-cpx geothermometer (Brey and Köhler 1990; Brey et al. 1990; Nimis and Taylor 2000).

Experimental details

Sample preparation

Thick slices were initially cut from each xenolith using a low speed saw. Each slice was then mounted in resin, ground and polished to generate the self-supporting, parallel-sided wafers to be used for infrared analysis. To minimize the possibility of preferred crystallographic orientation influencing the resulting averaged spectrum for each phase, sections were initially cut from the xenolith at different orientations relative to each other. Further, in order to ensure that the infrared beam would not be completely absorbed during infrared analysis, several wafers, each of a different thickness, were prepared for each xenolith. The thickness of the wafers varied according to sample and ranged between 100 and 500 (±5) μm. Wafer thicknesses were measured using a digital micrometer.

Rationale behind the spectroscopic approach

Both synchrotron μ-FTIR and black-body sourced μ-FTIR spectroscopy were used to identify and quantify hydroxyl in the individual xenolith phases. Crystals analysed using synchrotron FTIR were not oriented according to crystallographic axes. A linear relationship exists between the number of infrared active bonds in a system and the intensity of the resulting absorption and so, conversely, the intensity of an OH absorption band should be proportional to the concentration of the absorbing species. This, however, is not always the case as the measured intensity of OH absorptions also depends on the orientation of the IR active dipole relative to the incident radiation. Accurate quantitative measurement of absorbing species in anisotropic minerals therefore requires analyses of oriented single crystals using polarized IR radiation (Libowitzky

and Rossman 1996). Unfortunately performing such a procedure on natural rocks is extremely difficult and so here, where measurements were made using synchrotron μ-FTIR, we instead analysed a statistically significant number of individual crystals of each phase. Spectral data were then compiled to build an averaged spectrum for that phase in each sample. By doing this, intensity variations imposed by the relative geometric relationships between the OH dipole relative to crystallographic orientation are averaged out. After incorporating an orientation factor into the Beer-Lambert's law equation (Paterson 1982), the averaged spectrum was then used to estimate phase water contents. Most measurements using a traditional, black-body infrared source were collected on single crystals of each phase oriented according to crystallographic axes and using a polarised beam as described below. By comparing the total integrated OH absorbance from the averaged spectrum with that obtained on spectra obtained through polarised measurements a good measure of the accuracy of this averaged spectrum approach was attained.

Synchrotron FTIR μ-spectroscopy

Unpolarised absorbance spectra were collected using synchrotron FTIR μ-spectroscopy at the LURE synchrotron facility, Université Paris-Sud, France (MIRAGE beamline). A Nicolet 550 infrared spectrometer coupled with a NicPlan IR microscope was used to obtain room temperature infrared spectra in the region between 650 and 4,000 cm^{-1} at a spectral resolution of 4 cm^{-1}. Each spectrum was collected after 1,024 accumulations (total recording time per spectrum ~2 min). An adjustable aperture was available to determine the projected size onto the sample, depending upon the objective enlargement. In this study, we used a 32× objective, with a Numerical Aperture (N.A.) of 0.64. Projected aperture size as low as 6×6 and/or 3×3 μm^2 was routinely set without degrading the spectral quality (Signal-to-noise). Such small domain size enabled the accurate selection of regions of each crystal that appeared, under optical examination, to be clear of inclusions or fractures.

Polarized FTIR μ-spectroscopy

To complement the synchrotron-based experiments, polarized FTIR spectra were collected using a NicPlan and a Continuμm infrared microscopes and a Nicolet Nexus FTIR spectrometer. A Globar™ source, KBr beamsplitter, and dedicated liquid nitrogen-cooled MCT detector were used to measure 512 scans for each spectrum. Spectra were collected with a spectral resolution of 4 cm^{-1}. A ZnSe wire grid polarizer in the infrared microscope was used to polarise the incident radiation. Background spectra were collected immediately after sample collection with the polariser aligned in the same orientation as was used to collect the sample spectrum. Beam diameter was adjusted using an adjustable aperture located in the microscope. The minimum spot size attainable using adjustable apertures and the black body source is about 20×20 μm. Throughout the analytical procedure the spectrometer and the entire microscope unit was sealed in a Perspex box and evacuated by purging with dry air and nitrogen.

Clear grains of olivine and orthopyroxene were analysed using a polarised beam and the orientation of the crystal determined using the overtone modes of the silicate framework vibrations in the region 2,350–1,250 cm^{-1}. The method is described elsewhere (Jamtveit et al. 2001). Crystal alignment, which is estimated to be accurate to 10°, is sufficiently accurate for measuring OH band intensities on the resulting spectrum (Libowitzky and Rossman 1996).

Quantifying OH concentrations

A background was subtracted from all spectra by fitting a 3rd order polynomial. Occasionally, residual traces of epoxy C–H on sample wafers generated minor absorptions between 3,000 and 2,800 cm^{-1}. Analysing a different part of the crystal usually yielded a pure spectrum for that crystal, however, in a few cases traces of epoxy were found on all spectra from a sample. When this occurred, the contribution of the C–H bands was not considered in the calculation of the total integrated OH absorbance.

We attempted to resolve individual peaks on the background-subtracted spectrum of each phase using the Peakfit program (Jandel Scientific). Clinopyroxene and orthopyroxene spectra proved impossible to resolve accurately using this method as both required a greater number of peaks than were readily identifiable on the spectrum to generate a satisfactory solution. Resolving individual OH bands on olivine spectra proved more successful. Integrated absorbencies associated with OH in clinopyroxene and orthopyroxene were determined by integrating the entire region between 3,700–3,000 and 3,750–2,800 cm^{-1}, respectively. The total integrated OH absorbance in olivine was calculated by summing each peak resolved by peak fitting. OH concentrations in all phases were estimated from the total integrated absorbance using the Beer-Lambert law:

$$\text{Abs} = \varepsilon_i \cdot d \cdot \gamma \cdot \text{OH concentration}$$

Where, Abs represents the total sum of integrated absorbencies of the OH bands on the averaged IR spectrum, ε_i is the molar absorption coefficient, d is the thickness of the sample, and γ is the orientation factor (Paterson 1982). Experimentally determined values of ε_i for clinopyroxene,

orthopyroxene (Bell et al. 1995), and for olivine (Bell et al. 2003) were used. Olivine OH contents were also calculated using two further methods in which the integrated molar absorption coefficient for individual OH bands are calibrated as a function of the vibrational energy of the absorbance (Libowitzky and Rossman 1997; Paterson 1982). For calculations made using the synchrotron measurements an orientation factor of $\gamma = 1/3$ was incorporated into calculations of clinopyroxene, orthopyroxene, and olivine (Paterson 1982). In calculations where the sum of absorbencies measured with polarised light ($A^{tot} = A^{E\|x} + A^{E\|y} + A^{E\|z}$), $\gamma = 1$.

Choice of extinction coefficients

The extinction coefficient is used to calibrate the integrated OH absorbance to a concentration of absorbing species and can be derived from a number of sources. Mineral specific values for clinopyroxene, orthopyroxene and olivine are given in Bell et al. (1995, 2003). Wavenumber-dependant calibrations describe the calculation of a specific extinction coefficient for each band resolved on a spectrum (Libowitzky and Rossman 1997; Paterson 1982). OH absorbance spectra of clinopyroxene, orthopyroxene and garnet described in this study closely resemble those used to determine the mineral specific extinction coefficients (Bell et al. 1995). We have therefore calculated dissolved water contents of these three phases from the OH stretching spectrum using the relevant extinction coefficient. Although the OH absorption spectrum of olivine from the different xenoliths studied here varied (see Fig. 3), we chose to employ the mineral-specific absorption coefficient (Bell et al. 2003) to estimate the water contents in our samples, however, olivine water contents were also calculated using wavenumber-specific calibrations and these have been included for comparison (Table 3).

Results

Hydroxyl in mantle xenoliths

Infrared spectra of clinopyroxene, orthopyroxene and olivine from Kilbourne Hole (KHL8302, 8306 and 8308) and Barges (BAR 8303) contain absorptions attributed to OH species (Figs. 1, 2, 3). No OH was found in any of the spinel crystals analysed. Clinopyroxene, orthopyroxene and olivine crystals from garnet lherzolite xenoliths LMA15, LTP15 and KBJ30 contain numerous absorption bands, which are attributed to OH species. OH bands were found in orthopyroxene and olivine from B13 but no clinopyroxene crystals suitable for infrared analysis were found in this cpx-poor sample. Garnet crystals in each of the xenoliths contain numerous OH bands attributed to secondary hydrous phases (see below) but were otherwise anhydrous (Fig. 4). In each crystal studied the vibrational frequencies of the main OH absorbances are similar to those previously reported for each phase in the literature (Figs. 1, 2, 3). Polarised infrared spectra were also collected from oriented single crystals of olivine from KHL8306, B13, KBJ30 and LTP15 (Fig. 5) and orthopyroxene crystals from KHL8306, KBJ30 and LMA15.

Contamination by secondary phases

Crystals in the garnet peridotites were frequently interspersed with inclusions or fractures filled with high birefringence secondary impurities. Each point analysed using

Table 3 Integrated absorbencies and calculated hydroxyl contents in the studied xenoliths

	Cpx		Opx				Olivine								Whole rock
	$3*Abs_{av}$	OH_{av}^{B1}	$3*Abs_{av}$	OH_{av}^{B1}	Abs_{pol}	OH_{po}^{B1}	$3*Abs_{av}$	OH_{av}^{P}	OH_{av}^{L}	OH_{av}^{B2}	Ab_{pol}	OH_{pol}^{P}	OH_{pol}^{L}	OH_{pol}^{B2}	
BAR8303	2,931	**413**	2,985	**201**	–	–	30	2.3	3.2	**5.7**	–	–	–	–	**117**
KHL8302	2,874	**405**	2,628	**177**	–	–	14	1.6	1.2	**2.6**	–	–	–	–	**121**
KHL8306	2,517	**355**	2,502	**169**	2764	186	66	2.9	4.2	12.4	43.3	1.9	2.4	**8.1**	**100**
KHL8308	2,904	**409**	2,904	**196**	–	–	27	1.7	2.3	**5.1**	–	–	–	–	**109**
B13	–	–	2,790	**188**	–	–	69	6.2	8.8	**13.0**	120	10.2	14.3	22.6	**67**
KBJ30	2,829	**399**	2,961	**200**	2942	198	206	16	23	**38.7**	389	29.3	40.6	73.1	**113**
LMA15	2,427	**342**	2,691	**181**	3164	213	288	29	42	**54.1**	–	–	–	–	**135**
LTP15	2,655	**374**	2,667	**180**	–	–	40	3.8	5.4	**7.5**	13.2	1.2	1.6	2.5	**94**

Abs_{av} = total integrated OH absorbance measured from averaged unpolarized spectra (see text for details). Abs_{pol} = total OH absorbance summed from polarised spectra. $Abs_{pol} = A^{E\|x} + A^{E\|y} + A^{E\|z}$. OH contents calculated using extinction coefficients from ^{B1}Bell et al. (1995), ^{P}Paterson (1982), ^{L}Libowitzky and Rossman (1997) and ^{B2}Bell et al. (2003). The value thought to best estimate of the amount of H_2O in each phase is highlighted in bold. Whole Rock was estimated by multiplying the amount of H_2O in each phase by the modal composition of each xenolith (Table 1)

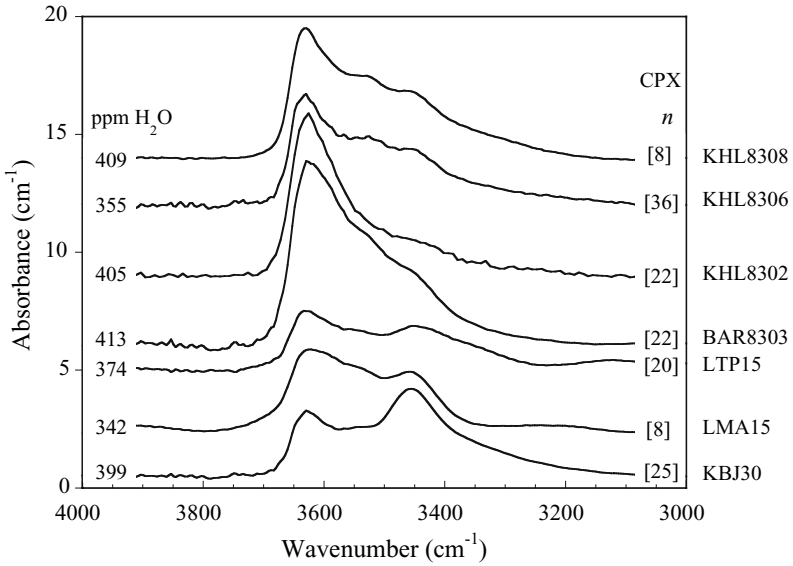

Fig. 1 Representative average infrared spectra of clinopyroxenes from each of the studied xenoliths. Spectra throughout have been normalised to 1 cm thickness and may have been offset vertically. *Numbers in square brackets* indicate the number of individual unoriented crystals analysed and averaged to obtain the spectrum from which the water contents were calculated. Respective water concentrations are printed on the left of each spectrum (see text for explanation)

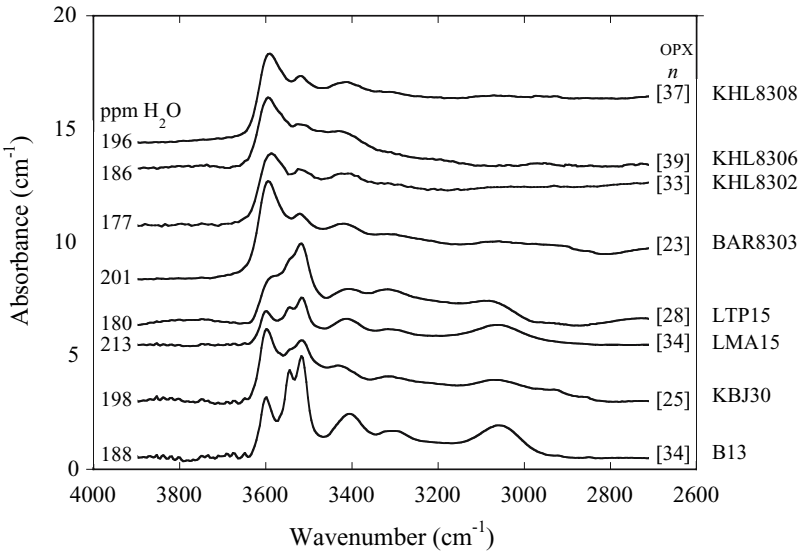

Fig. 2 Representative average infrared spectra of orthopyroxene

synchrotron FTIR was carefully selected so that the beam traversed the crystal along a path that appeared free of any inclusions or fractures. Despite this, sample spectra occasionally contained an intense, narrow band centred between 3,682 and 3,692 cm^{-1}. This absorption is not an intrinsic OH absorption for each phase, but was found on clinopyroxene, orthopyroxene, olivine and garnet spectra from the garnet-bearing samples B13, LMA15, LTP15 and KBJ30. The frequency and relative intensity of contaminant peaks such as these have been described previously (Jamtveit et al. 2001; Matsyuk and Langer 2004) and have been attributed to serpentine in the beam path. KBJ30 and B13 are visibly more heavily serpentinised. As the serpentine has been deemed the product of late stage alteration only spectra free of such inclusions were co-added to generate the averaged spectrum of the phase from which the water contents were subsequently calculated. No bands associated with secondary phases were observed in spectra from any of the spinel lherzolite xenoliths (KHL8302, KHL8306, KHL8308 and BAR 8303).

Clinopyroxene

Clinopyroxenes contain up to four readily identifiable OH absorptions (Fig. 1). Spectra from all xenoliths have three easily identifiable bands centred at 3,633, 3,540, and 3,456 cm^{-1}. Clinopyroxenes in LTP15 generate a further weak band centred between 3,325 and 3,370 cm^{-1}, which is also present as a shoulder on spectra collected on clinopyroxene each of the other localities. Using the total inte-

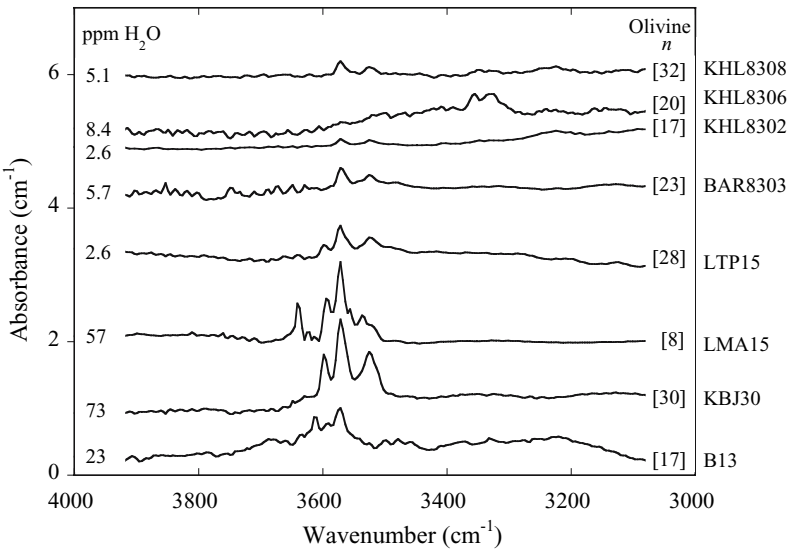

Fig. 3 Representative average infrared spectra of olivine

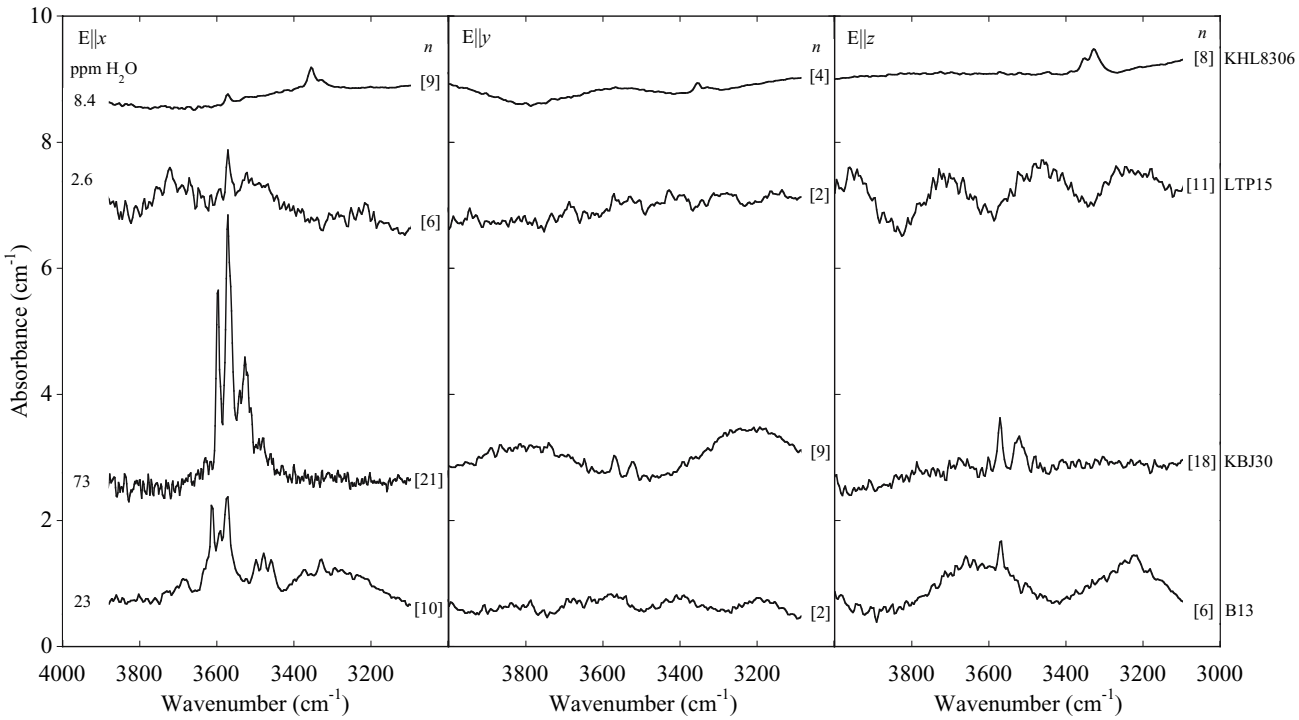

Fig. 4 Representative polarised infrared spectra of olivine from four of the studied xenoliths. *Numbers in square brackets* indicate the number of individual crystals on which polarised measurements were made. Water concentrations, printed on the left of spectra measured where $E\|x$, are those estimated using the mineral-specific absorption coefficient (Bell et al. 2003) and the total integrated OH absorbance (A^{tot}) summed from polarised measurements made parallel to each crystallographic direction ($A^{tot} = A^{E\|x} + A^{E\|y} + A^{E\|z}$)

grated OH absorption between 4,000 and 3,000 cm^{-1}, which was derived from the averaged clinopyroxene spectrum of each sample and the phase-specific OH absorption coefficient (Bell et al. 1995), clinopyroxene in the studied xenoliths contain between 342 and 413 ppm wt H_2O (Table 3). No discrimination between spinel and garnet lherzolites can be made using the total concentration of water in clinopyroxene from these xenoliths but an increase in the intensity of the OH band centred at 3,450 cm^{-1} relative to that centred at 3,633 cm^{-1} is systematic in garnet lherzolites (Fig. 1).

Orthopyroxene

The principle vibrations of OH-related defects in orthopyroxene from spinel lherzolites give rise to absorbance

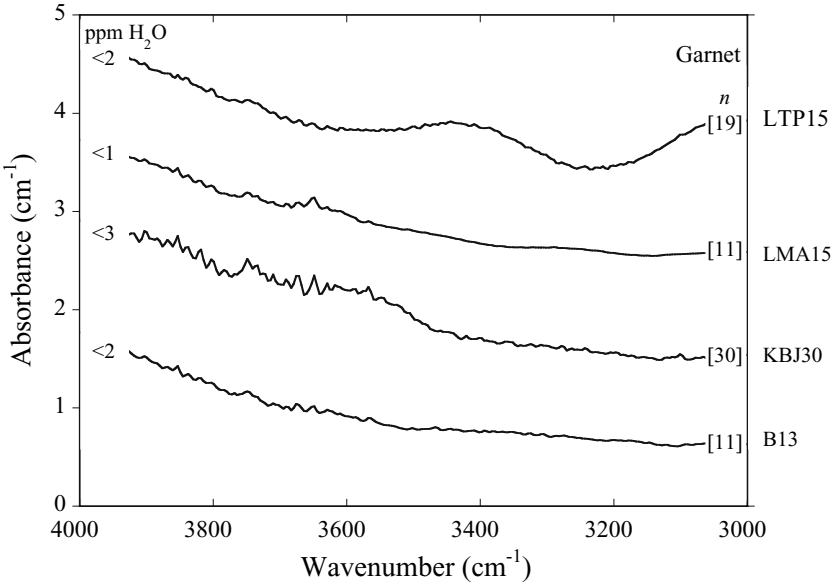

Fig. 5 Representative average absorbance spectra of garnet

bands between 3,605–3,590, 3,523–3,519, 3,422–3,397 and 3,060–3,080 cm^{-1} (Fig. 2). OH speciation is more complex in orthopyroxene from garnet peridotites than in crystals from the spinel-bearing samples and up to seven OH defect related absorbance bands could be identified in some spectra. The band centred between 3,523 and 3,519 cm^{-1}, apparent on spectra collected on opx from spinel lherzolites, splits into two separate bands, centred at 3,511–3,520 and 3,559–3,541 cm^{-1}, in spectra from garnet peridotites. This splitting is especially pronounced on spectra of orthopyroxene from xenoliths B13, LMA15 and KBJ30. Orthopyroxenes from each of the garnet peridotite xenoliths also frequently contain a more prominent band centred between 3,086 and 3,060 cm^{-1} and additional bands are found between 3,578 and 3,566 cm^{-1} (KBJ30, LTP15, and B13) and between 3,323 and 3,292 cm^{-1} (LMA15, LTP15, KBJ30, B13, KHL8308 and BAR8303). As is the case for the clinopyroxene crystals described above, OH bands between 3,550–3,500 and 3,422–3,397 cm^{-1} are larger relative to those centred at 3,605–3,590 cm^{-1} when orthopyroxene spectra from garnet peridotites are compared to those from spinel lherzolites.

Orthopyroxene water contents calculated from the sample-averaged spectrum and using Bell et al. (1995) range between 169 and 201 ppm H_2O. There is no systematic difference between the amount of water dissolved in orthopyroxene from spinel and garnet peridotites (Table 3). Water contents estimated from the total integrated OH absorbance obtained through polarised measurements are indistinguishable to those obtained using the averaged spectrum with a maximum deviation of 15% (Table 3).

Olivine

Averaged olivine IR absorption spectra are summarized in Fig. 3. Polarised absorption spectra of olivine from samples B13, KBJ30, LTP15 and KHL8306 are presented on Fig. 5. OH absorptions in olivine are complex but can be broadly classified into two groups according to vibrational energy (Bai and Kohlstedt 1993). Group I and II absorptions are found between 3,650–3,450 and 3,450 and 3,200 cm^{-1}, respectively. Spectra collected on olivine from BAR8303 and KHL8302 only show group I modes. Olivine from KHL8306 is dominated by OH modes in the group II region and olivine from the other spinel lherzolite samples contain both group I and II OH absorptions. These later samples generate spectra comprising two bands located at 3,576 and 3,528 cm^{-1} and two bands located at 3,358 and 3,330 cm^{-1}. Hydroxyl defects in olivine from B13, KJB30, LMA15 and LTP15 only generate group I modes. The number of individual OH modes comprising the group I region of the spectrum is greater in olivine from garnet lherzolites than for spinel lherzolites. In addition to the OH modes described for samples from spinel lherzolites, spectra of olivine from garnet lherzolites have extra bands at or above 3,598 cm^{-1} up to 3,640 cm^{-1}. These vibrations are coupled with minor concentrations of group II defect species in samples B13, KBJ30 and LTP15 (Fig. 5). Olivine from B13 also contains three further bands centred at 3,498, 3,480, and 3,455 cm^{-1}, which are strongly polarised parallel to the crystallographic *x*-axis (Fig. 5).

Olivine water contents were estimated using wavenumber-dependant (Libowitzky and Rossman 1997; Paterson 1982) and mineral-specific absorption coefficients (Bell et al. 2003) (Table 3). The olivine-specific integrated

absorption coefficient was calibrated using olivine crystals dominated by group I absorptions (Bell et al. 2003). Olivine from BAR 8303, KHL8302, KBJ30, LMA15, LTP15, B13 and KHL8308 are dominated by group I OH modes and so applying the mineral-specific calibration should give the best estimate of H_2O content. However, as it has been shown that the absorption coefficient likely varies as a function of band energy (Libowitzky and Rossman 1997; Paterson 1982), wholesale application of the mineral-specific calibration to samples that display a contribution from group II bands, such as olivine from sample KHL8306, could lead to erroneous water contents. To estimate the amount of water dissolved in olivine from KHL8306 using unpolarised spectra we decided to take the mean of the value obtained using the wavenumber-specific absorption coefficient (Libowitzky and Rossman 1997) and the olivine specific coefficient (Bell et al. 2003). This value is close to the 8.1 ppm H_2O estimated from the polarised infrared spectra (Table 3). Our best estimates of the amount of water dissolved in the mantle olivines studied are printed in bold in Table 3.

We also made polarised infrared absorbance measurements on at least ten different olivine crystals from each of the samples B13, KBJ30, LTP15 and KHL8306 (Fig. 5). Water concentrations calculated from polarised spectra are provided in Table 3. The amounts of water calculated using polarised absorbance spectra of samples KHL8306 and LTP15 are lower than those deduced from unpolarised spectra. Those made on polarised absorbance spectra are higher than those made from unpolarized spectra in samples B13 and KBJ30.

Garnet

Garnet crystals studied here are essentially anhydrous, or at least have very low water concentrations at the limit of infrared sensibility. Only lower limits of partition coefficients between clinopyroxenes and garnets can be estimated (Fig. 4).

Homogeneity of hydroxyl contents

Figure 6 shows FTIR spectroscopic profiles performed through single olivine grains contained in polished sections. Spectra were measured inwards from crystal edges at 25 and 50 μm intervals for six of the eight samples. For these measurements, we selected the most vertical and straight olivine edges available in the different thin sections. No zoning of OH content or a change of spectra was observed at the scale of the observations (Fig. 6). Slight zoning of dissolved water contents, measuring less than 150 μm in length, was observed at the edge of a single olivine from sample KHL8302. Such zoning was, however, not found in any other measurement performed in other olivines from this sample (Fig. 6). The low OH concentration in olivines from spinel lherzolites, especially sample KHL8302, necessitates the analysis of sample wafers several hundred microns thick. Thus, it is difficult to achieve a spatial resolution better than 100 μm in these samples. This probably also explains the apparent zoning observed at the rim of the single grain described above. Fractures or inclusions, which are common throughout the garnet lherzolites, render the use of linear traverses difficult. No profile was performed in samples KBJ30 and LTP15 but the spatial homogeneity of olivine crystals was assessed by comparing the integrated absorbance of OH absorptions measured at different points within olivine crystals. Repeated measurements made in all samples proved conclusively that the amount and speciation of water within individual crystals is spatially homogeneous regardless of position in the xenolith at least beyond 100 μm from the edges. FTIR micro-spectroscopy using a synchrotron light source allows significantly smaller surface areas to be analysed if the concentration of absorbing species is sufficiently great to allow the analysis of thin sections. Figure 7 shows profiles performed across the pyroxene-olivine interface of sample KHL8306 using a spot with resolution of 3×3 μm. These analyses show that no OH zoning was detectable in pyroxenes even at a resolution of tens of microns, and that no hydrous phase was detected at the grain boundary within this resolution.

We also checked the homogeneity of hydrogen contents of each phase throughout a sample xenolith. This was achieved by using polarised infrared spectroscopy to identify the overtone modes of the silicate lattice vibrations (Jamtveit et al. 2001). The integrated absorbance under the OH bands on the polarised infrared spectrum of a crystal was then compared to that obtained on different spectra collected along the same crystallographic orientation located throughout the same sample. The number of olivine crystals analysed in this way are outlined in Fig. 5. Integrated absorptions measured at different positions within the same xenolith were also identical (± <10%).

Distribution of water between phases and total water content

Mineral–mineral partition coefficients ($D_{\text{water}}^{\text{min–min}}$) were calculated to describe the distribution of water between coexisting clinopyroxene, orthopyroxene and olivine in the studied xenoliths (Table 4). Water solubility data deduced from average spectra were preferred to sparse polarised values when compiling the distribution coefficients. Water contents outlined in bold text on Table 3 were used to compile the distribution coefficients. As has been previously reported from studies of both natural and synthetic

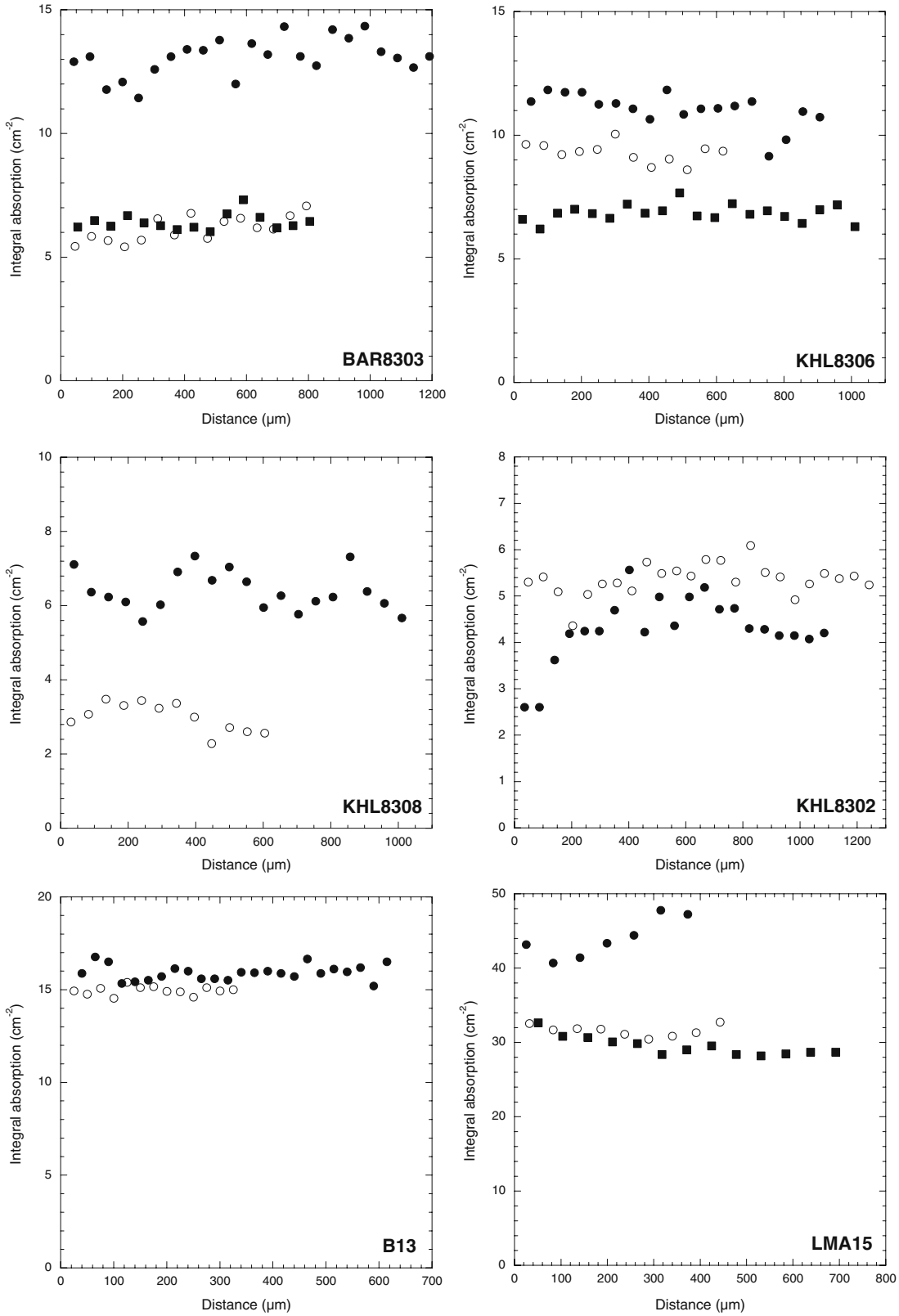

Fig. 6 Integrated OH absorbance intensities from unpolarised spectra collected within individual grains of olivine from six peridotite samples. The *y*-axis shows the integrated magnitude of OH bands at 3,576 and 3,528 cm^{-1} in olivine from BAR8803, KHL8302, KHL8308, B13 and those at 3,330–3,358 and 3,407 cm^{-1} in samples from KHL8306 and LMA15. The *x*-axis shows distance from the rim of the crystal (rim = 0 μm). Beam size was 20–50 μm. The uncertainty on measurements is estimated to 10%

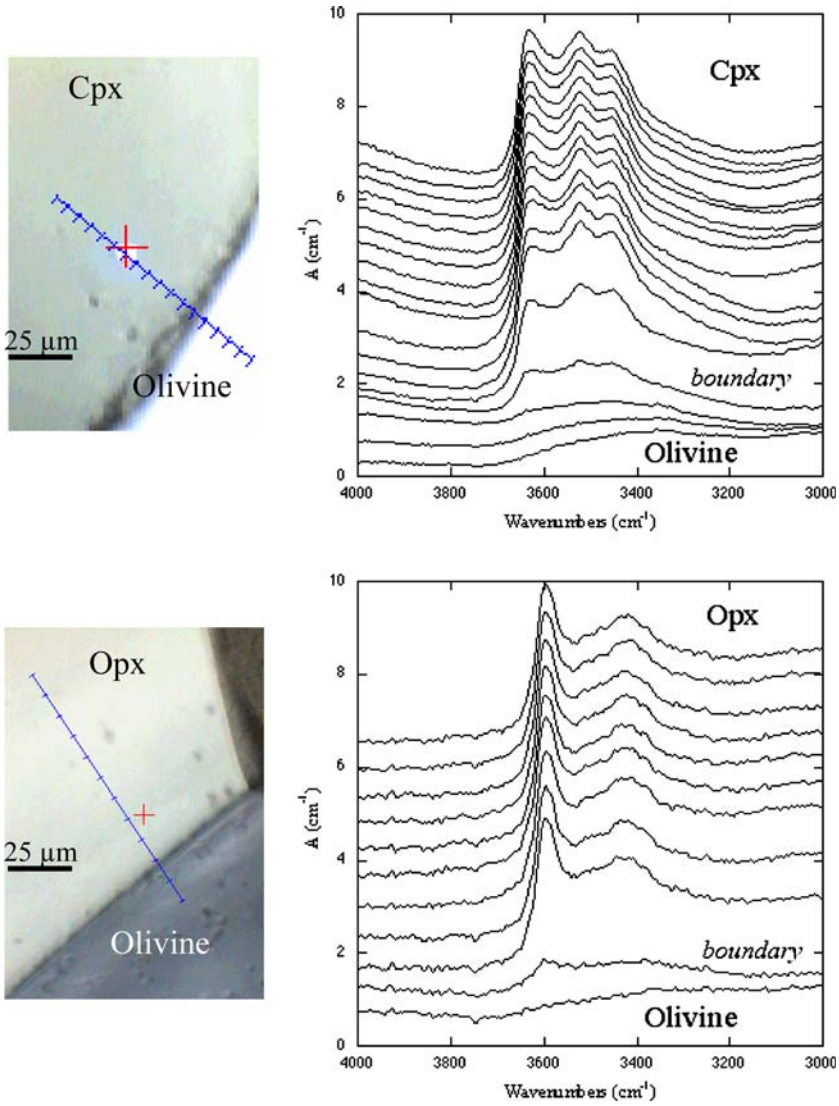

Fig. 7 Two representative, synchrotron FTIR profiles measured across mineral–mineral boundaries in sample KHL8306. Profiles show OH absorbances measured across a diopside–olivine and enstatite–olivine interface and were analysed using a spot size of 6 and 10 µm, respectively

systems (Aubaud et al. 2004; Bell and Rossman 1992a; Koga et al. 2003; Peslier et al. 2002) clinopyroxene OH contents correlate well with those in orthopyroxene ($D^{cpx-opx}_{water}$ = 1.9–2.3). The average distribution of hydrogen between clino- and orthoyroxene in the xenoliths varies only slightly $D^{cpx/opx}_{water}$ = 2.1 (±0.1) however, the range of $D^{cpx/oliv}_{water}$ varies significantly between spinel and garnet peridotite: the average values are $D^{cpx/oliv}_{water}$(spinel) = 88.1 ± 47.8 and $D^{cpx/oliv}_{water}$(garnet) = 22.2 ± 24.1, respectively. $D^{opx/oliv}_{water}$ also decreases from spinel to garnet peridotite: $D^{opx/ol}_{water}$(spinel) = 40.7 ± 19.8 in the former compared to $D^{opx/ol}_{water}$(garnet) = 11.7 ± 9.5 in the later. Garnet crystals studied here are essentially anhydrous, $D^{cpx/gt}_{water}$ is higher than 200 for most of the samples. A strong partitioning between pyroxenes and garnet has been also reported from pyroxene exsolutions within mantle garnets (Guilhaumou et al. 2005). Due to an increase in the amount

Table 4 Partition coefficients calculated between cpx, opx and olivine present in each of the studied xenoliths

	$D^{cpx/opx}_{OH}$	$D^{cpx/ol}_{OH}$	$D^{opx/ol}_{OH}$
BAR8303	2.1	72.5	35.3
KHL8302	2.3	156	68.1
KHL8306	2.1	43.8	20.9
KHL8308	2.1	80.2	38.4
Mean	2.1 ± 0.1	88.1 ± 47.8	40.7 ± 19.8
B13	–	–	14.5
KBJ30	2.0	10.3	5.2
LMA15	1.9	6.3	3.3
LTP15	2.1	49.9	24.0
Mean	2.0 ± 0.1	22.2 ± 24.1	11.7 ± 9.5
Mean (all samples)	2.1 ± 0.1		

of water dissolved in olivine in garnet peridotites the partition coefficients involving pyroxenes/olivine decrease by a significant factor (around × 4) at the spinel/garnet boundary while the partition coefficient between pyroxenes remains constant.

We estimated the total water content of each xenolith by multiplying the water content of individual minerals by the modal composition of the xenolith (Table 3). Total xenolith water contents do not correlate with depth of the sample and is broadly comparable for both types of xenoliths with an average value of 107 ± 21 ppm H_2O (113 ± 14 ppm H_2O if we exclude the cpx-deficient sample B13).

Discussion

Quantitative OH analysis using IR spectroscopy

We based our quantitative calculations on a mean spectrum calculated for a sample by averaging a large number of unpolarised analyses and we tested the validity of this approach by estimating the phase water contents of several samples using polarised measurements. Estimated water contents of pyroxene, obtained using both analytical methods, are identical: differences are less than the likely errors associated with fitting a background to pyroxene spectra (Koga et al. 2003). Olivine water contents calculated from averaged spectra deviate to different degrees from those calculated from polarised measurements (Table 3). Phase water contents calculated from polarised spectroscopic measurements on oriented single crystals are theoretically more accurate than those made on un-oriented samples. However, polarised measurements described here have poorer signal to noise ratio. This is perhaps the reason for the relatively higher differences between polarised and unpolarised measurements we describe. Water contents estimated using the two spectroscopic techniques vary by up to a factor 2 (Table 3), demonstrating that uncertainty in our estimated olivine water contents is quite high. As data from un-oriented analyses were all collected using identical analytical conditions we have used this to evaluate relative OH concentrations; especially because, except for sample KHL8306, olivine from all samples have comparable OH signatures (Fig. 3). Most importantly, the relative uncertainty in these estimates does not change the main conclusion that the amount of water dissolved in olivine is significantly greater in crystals from garnet peridotites when compared to those comprising spinel peridotites (Table 4).

Equilibrium of OH contents

Before one can accurately describe the distribution of an element between two minerals it must be demonstrated that the two phases are in thermodynamic equilibrium. This is often difficult to evaluate but several, strong, lines of evidence demonstrate that the water contents of each of the phases reported here indeed represent equilibrium distribution of water between them. Firstly, any two grains from the same xenolith are chemically identical and no major element compositional zoning was observed. Secondly, mineral-mineral contacts in each of the studied xenoliths are sharp and well defined (with the exception of a dark corona around many of the garnet crystals of samples B13). Such pronounced crystal interfaces are most apparent in spinel lherzolites, where spectral traverses programmed across vertical mineral boundaries show that there is no melt or additional phases between the major phases and that OH contents are spatially homogeneous within mineral grains (Figs. 6, 7). Heterogeneous water contents were never observed in any of the crystals studied. We conclude, therefore, that each of these observations comprehensively dictates that the water contents of each phase, and the major element chemistries, are in thermodynamic equilibrium.

OH distribution coefficients

Relatively few data exist which describe the partitioning of hydrogen between mineral phases in mantle assemblages. Water contents of a suite of natural pyroxenes from sub-arc mantle-derived spinel peridotites yield $D_{\text{water}}^{\text{cpx/opx}} = 2.2 \pm 0.5$ (1σ, $n = 17$) (Peslier et al. 2002) and the distribution of water between pyroxenes from megacryst suites gives comparable results, $D_{\text{water}}^{\text{cpx/opx}} = 2.0 \pm 0.3$ (1σ, $n = 11$) (Bell et al. 2004). Partition coefficients calculated from coexisting mineral pairs described in this study ($D_{\text{water}}^{\text{cpx/opx}} = 2.1 \pm 0.1$) are in accordance with those previously described. As suggested elsewhere (Bell et al. 2004) our data confirm that the partition coefficients between pyroxenes show no relationship with sample equilibration conditions over a large temperature and pressure range (900–1,400°C, 1 to ~7 GPa). Partition coefficients calculated here are, however, less similar to partition coefficients calculated from analyses of synthetic samples; $D_{\text{H}}^{\text{cpx/opx}} = 1.4 \pm 0.3$ ($n = 1$) (Aubaud et al. 2004) and $D_{\text{H}}^{\text{cpx/opx}} = 0.9$–$1.42$ ($n = 5$) (Hauri et al. 2006). Here, we have deliberately used different subscripts, $D_{\text{water}}^{\text{min/min}}$ and $D_{\text{H}}^{\text{min/min}}$ to discriminate between studies where data were collected using infrared spectroscopy and ion micro probe.

The distribution of water between pyroxenes and olivine from spinel lherzolite samples described here ($D_{\text{water}}^{\text{cpx/oliv}}(\text{sp}) = 88.1 \pm 47.8$; $D_{\text{water}}^{\text{opx/oliv}}(\text{sp}) = 40.7 \pm 19.8$) are comparable to those published elsewhere in the literature for spinel lherzolites: $D_{\text{water}}^{\text{opx/olivine}}$ from Bell and Rossman (1992b) is equal to 40 ± 4 (1σ, $n = 3$) if the estimated olivine water concentrations are 0.7 times

lower than those obtained using the more recent, mineral-specific calibration (see Bell et al. 2004). Hauri et al. (2006) describe $D_H^{cpx/oliv}$ values ranging from 9 to 21 ($n = 6$).

For garnet peridotites, the partition coefficients deduced for megacrysts by Bell et al. (2004) [$D_{water}^{cpx/olivine} = 3.0 \pm 0.5$ (1σ, $n = 11$) and $D_{water}^{opx/olivine} = 1.6 \pm 0.2$ (1σ, $n = 9$)] are much lower than ours ($D_{water}^{cpx/oliv}$(Gt) = 22.2 ± 24.1, $D_{water}^{opx/oliv}$(Gt) = 11.7 ± 9.5). As pyroxene water contents are similar in both studies, the cause of this discrepancy is attributed to higher amounts of water dissolved in megacryst olivine. If the same, mineral-specific calibration is used to quantify the amount of water in olivine, the average water content of the olivine megacrysts, around 150 ppm wt H_2O (Bell et al. 2004), is four to five times higher than that recorded in our garnet peridotites. Partition coefficients calculated from ion probe measurements of synthetic olivine, orthopyroxene and coexisting melt yield $D_H^{opx/olivine} = 12 \pm 4$ (2σ) (Koga et al. 2003), $D_H^{opx/ol} = 8.8 \pm 0.7$ ($n = 4$) (Aubaud et al. 2004). These values are closer to those calculated in this study from data collected on garnet peridotite phases than those from spinel peridotites, however, a further experimental study described a larger range of values ($D_H^{opx/olivine} = 1$–16 ($n = 9$) (Hauri et al. 2006)) thus illustrating that significant variation exists, even within samples synthesised in a carefully controlled environment.

In their study of megacrysts from the Monastery Kimberlite, Bell et al. (2004) observed a strong dependence of OH partitioning in garnet with X_{Mg}^{gt}. The amount of water dissolved in our garnets is very low, leading to partition coefficients between clinopyroxene and garnet higher than 100 in KBJ30 ($X_{Mg}^{gt} = 82.4$) and higher than 200 for the other samples ($X_{Mg}^{gt} \geq 85.5$). These values agree with the extrapolation of the trend measured by Bell et al. in garnets with X_{Mg}^{gt} lower than 80 (Fig. 11 in Bell et al. 2004).

OH in pyroxenes

Both the principle OH vibrations and the amounts of water measured in pyroxenes in this study are consistent with those reported from other localities throughout the world (Bell and Rossman 1992b; Peslier et al. 2002; Skogby et al. 1990; Skogby and Rossman 1989). However, our results indicate that OH species dissolved in mantle clinopyroxene change according to the host xenoliths mineralogy. For example, OH absorptions centred at 3,633 and 3,540 cm^{-1} are present in clinopyroxene from garnet peridotites and not from spinel peridotites. A further band at 3,456 cm^{-1} is always more intense in garnet-bearing samples (Fig. 1). Such a correlation between host rock mineralogy and OH defect speciation is enhanced when additional data from previous published studies are compiled. We note that the intensity of the OH mode at 3,456 cm^{-1} is very rarely greater than that of those at 3,633 or 3,540 cm^{-1} on spectra collected on clinopyroxene crystals from spinel peridotites (Peslier et al. 2002), and that this is true regardless of crystal orientation. When analyses are made with E ∥ γ and [001], the dominant OH modes observed on polarised spectra collected on clinopyroxene megacrysts from garnet peridotites from the Monastery kimberlite is a band at 3,456 cm^{-1} (Bell et al. 2004). Annealing experiments on diopside single crystals have shown that the magnitude of OH bands in this spectral region change under more reducing conditions (i.e. where experimental fO_2 is buffered by the reaction Fe–FeO) (Bromiley et al. 2004). We note that the magnitude of the OH modes at 3,456 cm^{-1} dominates clinopyroxene spectra from all garnet peridotites studied here (Fig. 1). These observations lead us to suggest that this may be a general feature of clinopyroxenes from all garnet peridotites. Furthermore, coupling this with experimental observations (Bromiley et al. 2004) we suggest that the nature of the OH defect population dissolved in the samples can be directly attributed to decreased oxygen fugacity in the garnet P–T field. Oxygen fugacity is known to decrease with depth in subcontinental lithospheric mantle and, most abruptly, as the spinel to garnet boundary is crossed (Canil et al. 1990; McCammon and Kopylova 2004; Wood et al. 1996; Wood and Virgo 1989; Woodland and Koch 2003). For instance, the average oxygen fugacity measured in spinel lherzolites from Kilbourne Hole is around FMQ 0.40 (Ionov and Wood 1992) whereas the oxygen fugacity measured in garnet peridotites from Bultfontein Mine, Matsoku and Jagersfontein kimberlites (from which B13, LMA15 and KBJ30 derived respectively) is FMQ 2.8 to FMQ 3.6 (Woodland and Koch 2003), only about 1.5 orders of magnitude above the value of the Fe–FeO oxygen buffer equilibrium.

OH defect speciation in orthopyroxene from spinel lherzolites samples also differs to that dissolved in crystals from garnet-bearing samples. An OH mode centred at 3,600 cm^{-1} is dominant in orthopyroxene crystals from spinel lherzolites. Orthopyroxene from garnet peridotites contain a significant contribution from different OH modes, located at approximately 3,520 cm^{-1}. Once again, when OH modes in orthopyroxene from spinel peridotites (Peslier et al. 2002) are compared with those of orthopyroxene megacrysts from garnet peridotites (Bell et al. 2004) a correlation between OH defect speciation and host rock mineralogy is observed. However, the cause of spectral differences in orthopyroxene is more difficult to constrain than clinopyroxene because the effect of oxygen fugacity on the OH stretching signature of orthopyroxene appears smaller than clinopyroxene (Rauch and Keppler 2002) and the incorporation of Al plays an important role

in controlling the OH contents of enstatite and the shape of the infrared spectra (Rauch and Keppler 2002; Stalder and Skogby 2002; Stalder 2004; Stalder et al. 2005). These experimental studies have shown that the OH absorbance spectrum of natural orthopyroxenes can be reasonably well reproduced in laboratory through synthesising Al-bearing enstatite crystals at high pressure. Orthopyroxene crystals synthesised in a water-saturated environment are cosmetically similar to those of natural mantle orthopyroxene but the total integrated OH absorbance is about ten times higher than for natural samples (Stalder 2004). Synthetic enstatite containing 1.17 and 5.85 wt% Al_2O_3, which are in terms of both the polarised infrared absorbance spectrum and measured Al_2O_3 contents analogous to those from LTP15 and BAR8303 studied here, contain 543 and 1,443 ppm H_2O, respectively (Stalder 2004). Water contents in orthopyroxene from LTP15 and BAR8303 contain significantly less water (180 and 201 ppm H_2O, respectively) and show no correlation between Al and water contents.

OH in olivine

The amount of water dissolved in the olivine we describe is in broad agreement with that previously described for mantle olivine and well below the upper limit of 200 ppm H_2O fixed by the width of the discontinuity at 410 km induced by olivine–wadsleyite transition (Wood 1995). The most water-rich mantle-derived olivine crystals described in the literature are those from the Monastery Kimberlite (Bell et al. 2004). These samples, which may contain in excess of 250 ppm H_2O, are thought to have crystallised from magma or fluid enriched in volatiles and incompatible elements at high-pressure (Bell et al. 2004).

In this study, olivine crystals containing the greatest concentration of dissolved hydroxyl species are those from garnet peridotites. This corresponds with previous studies where it has been demonstrated that olivine from kimberlite xenoliths commonly contain more dissolved water and also frequently exhibit more complex OH absorbance spectra (Miller et al. 1987; Bell et al. 2003, 2004; Matsyuk and Langer 2004). The OH defect population in olivine from garnet peridotites is characterised by numerous absorptions between 3,650 and 3,450 cm^{-1} (Fig. 3). Spectra collected from olivine crystals from spinel peridotites generally contain fewer OH modes between 3,650 and 3,400 cm^{-1}, but may contain additional OH absorptions between 3,400 and 3,000 cm^{-1} (Miller et al. 1987; Jamtveit et al. 2001; Bell et al. 2003; Matveev et al. 2005). We note that, for the samples described here, an increase in the amount of water dissolved in olivine from garnet-bearing xenoliths is correlated with an increase of the number and complexity of OH modes found between 3,650 and 3,450 cm^{-1}. This observation correlates well with recent experimental studies (Berry et al. 2005) which suggest that, at pressures corresponding to those of spinel stability field, the equilibrium water content of olivine was limited by incorporation of hydrogen species associated with Ti-clinohumite-type defects. At higher pressures, approaching those where garnet becomes stable, OH-clinohumite would become the stable defect species and, accordingly, the dominant mechanism of incorporating water in olivine under this pressure regime (Berry et al. 2005). Clinohumite has more sites available for protonation than Ti-clinohumite, thus accounting for the more complex OH stretching signatures described for olivine from garnet-bearing rocks when compared to those from spinel-bearing samples (Berry et al. 2005). The different OH stretching signatures we describe here for olivine from the two stability fields correspond well with the results of the experimental study (Berry et al. 2005). Furthermore, the proposed difference in OH speciation also provides a plausible mechanism to accommodate the increased water contents of olivine from this field.

OH defects with vibrational modes in the energy range 3,400–3,000 cm^{-1} are relatively common in olivine from shallower regions of the upper mantle (Bell and Rossman 1992b; Khistina et al. 2002; Matveev et al. 2005). Despite this, the dominant mechanisms involved in their development remain uncertain. Two different possibilities have been proposed. The first is that OH modes between 3,380 and 3,285 cm^{-1} may develop as a function of SiO_2 activity (Matveev et al. 2001, 2005; Lemaire et al. 2004). In this model, OH modes at high and low energies are ascribed to silicon and metal vacancies respectively and the prevalence of one defect species over another was controlled by the silica activity of the system in which the crystal re-equilibrated. However, this relationship does not correspond with the results of other experimental studies and it has proven difficult reproduce in subsequent work (Zhao et al. 2004; Berry et al. 2005; Mosenfelder et al. 2006a, b). More recently, it has been suggested that low energy OH modes are likely associated with the substitution of trivalent cations in the olivine crystal lattice (Berry et al. 2005, 2006; Grant et al. 2006) and a correlation between the intensity of OH absorptions in this region with fO_2 has also been proposed (Matsyuk and Langer 2004; Mosenfelder et al. 2006a).

OH absorbance spectra collected on olivine from the three different Kilbourne Hole xenoliths studied here show that the relative intensity of the low energy OH modes differs in each (Fig. 3). No correlation exists between the OH defect speciation in olivine from the Kilbourne Hole xenoliths and ambient *P–T* conditions (Table 1). This implies that OH modes at 3,355 and 3,325 cm^{-1} do not develop or disappear gradationally as a function of depth.

Furthermore, regardless of the precise mechanism involved in the development of the low-energy modes (i.e. silica activity, Matveev et al. 2001, 2005 or in relation to trivalent cations in the crystal structure, Berry et al. 2005, 2006; Grant et al. 2006), different OH species dissolved in olivine crystals from different xenoliths from the same locality must imply that the concentrations of the corresponding defect populations cannot be totally controlled by the host melt.

Origin of the recorded xenolith water contents

Crystallographically bound hydrous defect species have been commonly reported in a huge range of mantle-derived samples from a variety of tectonic settings and numerous geographic localities. However, whether these samples can be used as a probe with which one can describe the amount and speciation of water in the mantle remains an unanswered question. This is largely because, at high temperature and under laboratory conditions, hydrogen diffuses extremely rapidly through pyroxene, olivine and garnet (Mackwell and Kohlstedt 1990; Ingrin et al. 1995; Wang et al. 1996; Hercule and Ingrin 1999; Blanchard and Ingrin 2004; Kurka et al. 2005; Demouchy and Mackwell 2006; Ingrin and Blanchard 2006; Stalder and Behrens 2006). Thus, it has been repeatedly suggested that hydrous species dissolved mantle-derived silicate phases re-equilibrate with the host melt during ascent and any information about the composition of the sample at ambient conditions is overprinted. However, convincing evidence that mantle-derived samples have actually lost water during ascent remains sparse and we note that in both of the two recent studies where heterogeneous water contents in mantle-derived olivine were interpreted as evidence for such a process of dehydration (Demouchy et al. 2006; Peslier and Luhr 2006) pyroxene crystals co-existing with the zoned olivine contain homogeneous water contents. This observation is extremely difficult to be satisfactorily explained by dehydration during ascent because hydrogen diffuses through pyroxenes and olivine at very similar rates (Ingrin and Skogby 2000; Stalder and Skogby 2003; Ingrin and Blanchard 2006; Ingrin and Grant 2006). Pyroxene co-existing with olivine crystals containing spatially heterogeneous water contents that were inherited by dehydration during ascent should also be zoned. At the same time, however, convincing evidence that mantle-derived samples retain hydroxyl species from mantle conditions are also rare, although several previous studies have suggested that the water contents of some mantle minerals may remain unaffected by late stage processes (Matsyuk et al. 1998; Peslier et al. 2002; Bell et al. 2004).

A suitable model, which can easily resolve this apparent paradox, can be constructed if the diffusion of different defect species in nominally anhydrous are considered independently. The speciation and amount of water dissolved in olivine can be changed from that inherited at mantle conditions through the diffusion of hydrogen, metal vacancies and/or cations (Kohlstedt and Mackwell 1998; Ingrin and Blanchard 2006). Hydrogen is by far the fastest diffusing species and moves extremely rapidly through the crystal lattice of olivine and pyroxenes (Ingrin and Blanchard 2006). Hydrogen incorporation into olivine through the redox exchange reaction is rate limited only by the diffusivities of polarons and protons (Mackwell and Kohlstedt 1990; Demouchy and Mackwell 2006; Ingrin and Blanchard 2006). The absolute number of protons dissolved in crystals of olivine and pyroxene are susceptible to change when entrained in a melt because the dominant force driving re-equilibration via the redox exchange reaction in olivine and pyroxene is fH_2O (Kohlstedt and Mackwell 1998; Ingrin and Grant 2006). Thus spatially homogeneous water contents dissolved in each of the crystals described in this study indicate equilibrium through hydrogen diffusion was attained in all of the samples and remained through the last phase of eruption.

Ultimately however, the number and speciation of OH defects dissolved in any crystal of olivine or pyroxene is not controlled by the diffusion of hydrogen but the concentrations of other crystallographic point defect species, such as those associated with cation vacancies, impurity substitutions or interstitials. The mobility of these point defects through the crystal lattice is slower than that of hydrogen diffusion—the relative rates of hydrogen diffusion coupled with cation vacancy and cation diffusion in olivine generally differ by several orders of magnitude on a wide range of temperature (Ingrin and Skogby 2000; Matveev et al. 2001, 2005; Demouchy and Mackwell 2006; Zhao et al. 2004; Ingrin and Blanchard 2006). Three separate lines of evidence in the data we describe in this study suggest that the studied xenoliths were entrained and cooled fast enough to preserve point defect concentrations inherited at ambient conditions.

Firstly, hydroxyl speciation in pyroxene from spinel and garnet-bearing samples is different, and following experimental studies (Rauch and Keppler 2002; Bromiley et al. 2004), these differences correspond with the anticipated change in ambient fO_2 associated with the change in facies with depth. Secondly, OH defect speciation is different in olivine crystals from spinel and garnet peridotites and, again, spectral differences correspond with the results of experimental studies (Berry et al. 2005). Thirdly, despite the fact that they were brought to the surface by identical magmas, OH defect speciation between 3,400 and 3,000 cm^{-1} in olivine from three different xenoliths from the same locality (KHL8306 versus KHL8302 and KHL8308) are slightly, but significantly, different. This

suggests that each of these three xenoliths must derive from geochemically distinct regions of the sub-continental lithosphere and the crystal defect population inherited there remains intact throughout entrainment and cooling. Redox exchange reactions are not able to modify OH speciation. Therefore, whatever mechanism is invoked to explain the development of low frequency OH modes in these olivines (Bai and Kohlstedt 1993; Matveev et al. 2001, 2005; Berry et al. 2005, 2006) OH defect species would have to undergo re-equilibration via a process of cation or cation vacancy diffusion. Wood and Virgo (1989) have already demonstrated that a large range of chemical compositions could be found within a relatively small suite of xenoliths from Kilbourne Hole. Thus, we believe that the most likely scenario to account for the spectra variability observed between olivine crystals from Kilbourne Hole is that the xenoliths have preserved the OH defect population inherited at mantle conditions prior ascent and cooling.

Water solubility in enstatite has been measured experimentally (Mierdel and Keppler 2004). These authors showed that ($C_{opx} = A{\cdot}f_{H_2O}{\cdot}\exp$ ($-\Delta H^{1bar}/RT$) $\exp(-\Delta V^{solid} P/RT)$, where C_{opx} is water solubility, f_{H_2O} the water fugacity, A, a constant equal to 0.01354 ppm/bar, ΔV^{solid} = 12.1 cm^3/mol the volume change of enstatite during incorporation of OH and ΔH^{1bar} = –4.563 kJ/mol, the reaction enthalpy at 1 bar (Mierdel and Keppler 2004). Thermodynamic controls on the solubility of water in clinopyroxene remain poorly constrained (Bromiley et al. 2004), however, as the samples described here and those of previous studies (Bell and Rossman 1992b; Peslier et al. 2002; Bell et al. 2004) show, water distribution between orthopyroxene and clinopyroxene is relatively constant. This suggests that factors controlling water solubility in clinopyroxene are likely similar to those of enstatite. C_{opx}/C_{cpx} does not change with f_{H_2O}, P and T (Table 3). Therefore, ΔH^{1bar}, ΔV^{solid} and the dependence of water solubility on f_{H_2O}, outlined following experimental studies of orthopyroxene, should also apply to mantle clinopyroxene. Despite this, however, our results demonstrate that the OH stretching signature of the pyroxenes record differences in the fO_2 of the source. The solubility of water in olivine also increases as a function of f_{H_2O} (Kohlstedt et al. 1996; Zhao et al. 2004) and ΔV^{solid} is equal to 10 cm^3/mol. ΔV^{solid} is, therefore, comparable to enstatite (Mierdel and Keppler 2004) but ΔH^{1bar} is around to 40 kJ/mol for mantle olivine (much greater than enstatite). This should translate to a steadily decreasing $D^{opx/ol}_{water}$ with depth. It cannot, however, satisfactorily explain the sharp decrease of $D^{opx/ol}_{water}$ our data suggest occurs at the spinel-garnet phase boundary. If, as suggested by the data described in this study and recent experimental work (Berry et al. 2005), water solubility in olivine from garnet peridotite field is greater in olivine from spinel peridotites, a critical parameter (extrinsic defect substitutions, pO_2, olivine non-stoichiometry with SiO_2 activity, TiO_2 content...) is missing from the most recent thermodynamic laws describing water solubility in mantle olivine (Kohlstedt et al. 1996; Zhao et al. 2004). Experimental data also show that, at constant f_{H_2O}, the amount of water dissolved in olivine and diopside is greater if samples have been pre-annealed in more oxidizing conditions (Bai and Kohlstedt 1993; Guilhaumou et al. 1999). This contradicts observations in natural samples where pyroxene and olivine from relatively more reduced spinel lherzolites generally have higher concentrations of dissolved water (Peslier et al. 2002; Peslier and Luhr 2006). Further analyses of water species dissolved in natural samples and additional experimental data are clearly needed to resolve this apparent paradox.

Because we have shown that the defect populations dissolved in the xenolith phases are representative of those at ambient conditions, at fixed $>f_{H_2O}$, distribution of the OH defect populations dissolved in the peridotite phases can also be used as a proxy for hydroxyl contents. The average amount of water dissolved in olivine from garnet peridotites is approximately a factor of 4 greater than that measured in olivine from spinel peridotite. As described above, it is well known that oxygen fugacity decreases as the spinel to garnet peridotite transition is crossed. Following a detailed study of OH partitioning in megacrysts from the monastery kimberlite Bell et al. (2004) suggested that, ''despite the high diffusivities of hydrous components in olivine, pyroxenes and garnet, these minerals preserve a signature that was established in their mantle source''. We suggest that, because we describe different OH defect populations according to the host rock mineralogy that the measurements described in this study confirm this conclusion. It is not yet clear, however, if OH concentrations in the lithospheric mantle source differ significantly to those acquired during deep re-equilibrium of xenoliths with the host magma. Regardless of the precise origin, however, our data strongly suggest that the mechanism of incorporating water in olivine differs substantially in crystals from spinel and garnet peridotites.

Water in lithospheric subcontinental mantle and possible geophysical implications

The arguments outlined above indicate that water speciation in the xenolith phases are representative of those in the subcontinental lithospheric mantle conditions. Water storage in pyroxene does not change across the spinel to garnet transition. However, our samples, and previous experimental studies (Berry et al. 2005), demonstrate that the mechanism by which water is incorporated into olivine is different in the spinel and garnet stability fields. We have shown that, at a fixed f_{H_2O}, the defect population dissolved

in olivine from garnet lherzolites accommodates approximately four times more hydroxyl than that in crystals from spinel lherzolites. However, this increase is not reflected in the whole rock water contents because an increase in the amount of water in olivine from garnet lherzolites is compensated by the relative decrease of the proportion of diopside in these samples.

An increase in the amount of water dissolved in olivine in the garnet stability field will have important implications on the plastic deformation and electrical conductivity of the sub-continental lithosphere. Plastic deformation of olivine is enhanced by water: creep laws determined from experiments show that strain rate is almost proportional to water fugacity (Mei and Kohlstedt 2000a, b; Hirth and Kohlstedt 2003). Water fugacity also controls the amount of water dissolved in mantle olivine through a linear relationship (Kohlstedt et al. 1996; Mosenfelder et al. 2006a, b). Because ambient water fugacity controls both of these parameters, the anticipated increase in dissolved hydrous species in olivine as the spinel-garnet transition is crossed, must be reflected in the viscosity of the subcontinental lithospheric mantle. Thus, the greater complexity in OH defect speciation we note in olivine from garnet peridotites could translate to a fourfold decrease in the viscosity of garnet facies compared to the spinel stability field. This anticipated decrease in viscosity, which is derived through simple linear extrapolation of the available data may, however, ultimately be limited by an increase in the viscosity of olivine as oxygen fugacity decreases. Such a relationship has been observed in dunite deformation experiments (Keefner et al. 2005). We have illustrated that the OH defect concentrations measured in our peridotite xenoliths were inherited at mantle conditions. Thus, the defect populations we describe are also those which control the plastic deformation of olivine under these conditions. Furthermore, as current experimentally determined solubility laws cannot adequately explain why we observe the different water distribution coefficients we describe between rocks from the spinel and garnet facies and quantify simultaneously the effect of oxygen and water fugacity on creep laws we suggest that water distribution coefficients should be employed to more accurately estimate the change of intrinsic point defects in olivine in different facies and the corresponding effect on the plastic deformation rate of olivine. Our measurements suggest that, for the same temperature and water fugacity, the average viscosity of garnet peridotite is lower than the viscosity of spinel peridotite by 0.2–0.6 log units for dislocation and diffusion creep respectively (Dixon et al. 2004). These values are comparable to the resolution of viscosity profiles deduced from modelling of isostatic adjustments (Kaufmann and Amelung 2000) but if it is proved to be a general feature the consequences for mantle dynamics are extremely important.

If we assume that hydrogen ions are responsible for the conductivity of olivine in the mantle, as suggested by numerous studies (Karato 1990; Bahr and Duba 2000; Huang et al. 2005), the increased hydrogen solubility at the spinel/garnet transition will also increase mantle conductivity. According to the Nernst–Einstein equation the conductivity is proportional to the concentration and the diffusivity of the involved charge carrier. Huang et al. (2005) suggested that, for olivine polymorphs, the main charge carriers are free protons and the conductivity, σ, is proportional to C_{ol}^{r} with C_{ol} the water concentration and $r = 3/4$ (in this model, σ is also proportional to $f_{\mathrm{O}_2}^{-1/8}$). Thus, the average electrical conductivity should increase by a factor of 3–7 at the spinel/garnet transition depending on whether or not we omit the effect of $f\mathrm{O}_2$ change. This change is very important compared to the average increase of the conductivity in the upper mantle, generally of the order of one log unit down to the transition zone (Utada et al. 2003) and is surely a major effect if the contribution of pyroxene conductivity is confirmed to be weak (Ruedas 2006). Conductivity models of the upper mantle are highly sensitive to the number and position of layers used in data inversion; the occurrence of a jump of conductivity at the spinel/garnet transition can serve as a base to minimize the number of parameters necessary for such modelling. For instance, the spinel/garnet transition can be used to explain the high-conductivity observed at 100 km depth below the Basin and Range as well as in other extensional settings (Egbert and Booker 1992; Lizarralde et al. 1995).

Acknowledgments Michèle Glücklich-Herbas kindly provided the spinel lherzolites samples. We thank Anton Beran who gave us access to its infrared microscope facilities for a preliminary analyses of some of the xenoliths. We also thank R. Stalder and an anonymous referee for their helpful comments. This study was supported by the EU, through the Human Potential Program HPRM-CT-2000-0056.

References

Aubaud C, Hauri EH, Hirschmann MM (2004) Water partition coefficients between nominally anhydrous minerals and basaltic melts. J Geophys Res 31:L20611. doi:10.1029/2004GL021341

Bai Q, Kohlstedt DL (1993) Effects of chemical environment on the solubility and incorporation mechanism for hydrogen in olivine. Phys Chem Miner 19:460–471

Bahr K, Duba A (2000) Is the asthenosphere electrically anisotropic? Earth Planet Sci Lett 178:87–95

Bell DR, Rossman GR (1992a) The distribution of hydroxyl in garnets from the subcontinental mantle of southern Africa. Contrib Mineral Petrol 111:161–178

Bell DR, Rossman GR (1992b) Water in the Earth's upper mantle, the role of nominally anhydrous minerals. Science 255:1391–1397

Bell DR, Ihinger PD, Rossman GR (1995) Quantitative analysis of trace OH in garnet and pyroxenes. Am Mineral 80:465–474

Bell DR, Rossman GR, Maldener J, Endisch D, Rauch F (2003) Hydroxide in olivine: a quantitative determination of the

absolute amount and calibration of the IR spectrum. J Geophys Res 108:2105. doi:10.1029/2001JB000679
Bell DR, Rossman GR, Moore RO (2004) Abundance and partitioning of OH in a high pressure magmatic system: megacrysts from the Monastery Kimberlite, South Africa. J Petrol 45:1539–1564
Berry AJ, Hermann J, O'Neill H, St C, Foran GJ (2005) Fingerprinting the water site in mantle olivine. Geology 33:869–872
Berry AJ, O'Neill H, St C, Hermann J, Scott DR (2006) The infrared signature of water associated with trivalent cations in olivine. Geochim Cosmochim Acta 70:A49–A49
Bertrand P, Mercier J-CC (1985) The mutual solubility of coexisting ortho- and clinopyroxene: toward an absolute geothermometer for the natural system? Earth Planet Sci Lett 76:109–122
Blanchard M, Ingrin J (2004) Hydrogen diffusion in Dora Maria Pyrope. Phys Chem Miner 31:593–605
Brey GP, Köhler T (1990) Geothermobarometry in four-phase lherzolites II. New thermobarometers and practical assessment of existing thermobarometers. J Petrol 31:1353–1378
Brey GP, Köhler T, Nickel KG (1990) Geothermobarometry in four phase lherzolites I. Experimental results from 10 to 60 kb. J Petrol 31:1313–1352
Bromiley GD, Keppler H, McCammon C, Bromiley FA, Jacobsen SD (2004) Hydrogen solubility and speciation in natural, gem-quality chromian diopside. Am Mineral 89:941–949
Canil D, Virgo D, Scarfe CM (1990) Oxidation state of mantle minerals from British Columbia, Canada. Contrib Mineral Petrol 104:453–462
Demouchy S, Mackwell SJ (2006) Mechanisms of hydrogen incorporation and diffusion in iron-bearing olivine. Phys Chem Miner 33:347–355
Demouchy S, Jacobsen SD, Gaillard F, Stern CR (2006) Rapid magma ascent recorded by water diffusion profiles in mantle olivine. Geology 34:429–432
Dixon JE, Dixon TH, Bell DR, Malservisi R (2004) Lateral variation in upper mantle viscosity: role of water. Earth Planet Sci Lett 222:451–467
Dumas P, Miller L (2003) The use of synchrotron infrared microspectroscopy in biological and biomedical investigations. Vib Spectrosc 32:3–21
Egbert D, Booker JR (1992) Very long period magnetotellurics at Tucson observatory: implications for mantle conductivity. J Geophys Res 97:15099–15112
Grant KJ, Kohn SC, Brooker RA (2006) The partitioning of water between olivine, orthopyroxene and melt in the system Albite-Forsterite-H_2O. Earth Planet Sci Lett (In press)
Griffin W, Sobolev NV, Ryan CG, Pokilhenko NP, Win TT, Yefimova ES (1999) Cr-pyrope garnets in the lithospheric mantle. I, compositional systematics and relations to tectonic settings. J Petrol 40:679–704
Guilhaumou N, Dumas P, Ingrin J, Carr GL, Williams GP (1999) Synchrotron infrared microspectroscopy applied to petrology in micron scale range. Internet J Vib Spectrosc 3:1–13
Guilhaumou N, Sautter V, Dumas P (2005) Synhrotron FTIR microanalysis of volatiles in melt inclusions and exsolved particles in ultramafic deep-seated garnets. Chem Geol 223:82–92
Hauri EH, Gaetani GA, Green TH (2006) Partitioning of H_2O between mantle minerals and silicate melts. Earth Planet Sci Lett 248:715–734
Hercule S, Ingrin J (1999) Hydrogen in diopside: diffusion, extraction-incorporation, and solubility. Am Mineral 84:1577–1587
Hirth G, Kohlstedt DL (1996) Water in the oceanic upper mantle: implications for rheology, melt extraction and the evolution of the lithosphere. Earth Planet Sci Lett 144:93–108
Hirth G, Kohlstedt DL (2003) Rheology of the upper mantle and the mantle wedge: a view from the experimentalists. In: Inside the subduction factory, Geophysical Monograph, American Geophysical Union, vol 138, pp 83–105
Huang X, Xu Y, Karato S-I (2005) Water content in the transition zone from electrical conductivity of wadsleyite and ringwoodite. Nature 434:746–749
Ingrin J, Blanchard M (2006) Diffusion of hydrogen in mantle minerals. In: Keppler H (ed) Volume 62. Mineralogical Society of America, Washington D.C., pp 291–320
Ingrin J, Grant KJ (2006) H profiles in mantle xenoliths: constraints from diffusion data. Geochim Cosmochim Acta 70:A277–A277
Ingrin J, Skogby H (2000) Hydrogen in nominally anhydrous upper-mantle minerals: concentration levels and implications. Eur J Mineral 12:543–570
Ingrin J, Hercule S, Charton T (1995) Diffusion of hydrogen in diopside: results of dehydration experiments. J Geophys Res 100:15489–15499
Ionov DA, Wood BJ (1992) The oxidation state of subcontinental mantle: oxygen thermobarometry of mantle xenoliths from central Asia. Contrib Mineral Petrol 111:179–193
Jamtveit B, Brooker RA, Brooks K, Lersen LM, Pederson T (2001) The water content of olivines from the North Atlantic Volcanic Province. Earth Planet Sci Lett 186:401–415
Karato S (1990) The role of water in the electrical conductivity of the upper mantle. Nature 347:272–273
Kaufmann G, Amelung F (2000) Reservoir-induced deformation and continental rheology in vicinity of lake Mead, Nevada. J Geophys Res 105:16341–16358
Keefner JW, Mackwell SJ, Kohlstedt DL (2005) Dunite viscosity dependence on oxygen fugacity. Lunar Planet Sci Conf, Houston, p 36
Khistina NR, Wirth R, Andrut M (2002) Modes of OH^- occurrence in mantle olivine. I. Structural hydroxyl. Geochem Int 40:332–342
Koga K, Hauri E, Hirschmann M, Bell DR (2003) Hydrogen concentration analyses using SIMS and FTIR: comparison and calibration for nominally anhydrous minerals. Geochem Geophys Geosyst 4:1019. doi:10.1029/2002GC00378
Kohlstedt DL, Mackwell SJ (1998) Diffusion of hydrogen and intrinsic point defects in olivine. Zeitschrift Physikalische Chemie 207:147–162
Kohlstedt DL, Keppler H, Rubie DC (1996) Solubility of water in the α-phase, β-phase and γ-phase of $(Mg,Fe)_2SiO_4$. Contrib Mineral Petrol 123:345–357
Kurka A, Blanchard M, Ingrin J (2005) Kinetics of hydrogen extraction and deuteration in grossular. Mineral Mag 69:359–371
Lemaire C, Kohn SC, Brooker RA (2004) The effect of silica activity on the incorporation mechanisms of water in synthetic forsterite: a polarised infrared spectroscopic study. Contrib Mineral Petrol 147:48–57
Libowitzky E, Rossman GR (1996) Principles of quantitative absorbance measurements in anisotropic crystals. Phys Chem Miner 23:319–327
Libowitzky E, Rossman GR (1997) An IR absorption calibration for water in minerals. Am Mineral 82:1111–1115
Lizarralde D, Chave A, Hirth G, Schultz A (1995) Northeastern Pacific mantle conductivity profile from long-period magnetotelluric sounding using Hawaii-to-California submarine cable data. J Geophys Res 100:17837–17854
Mackwell SJ, Kohlstedt DL (1990) Diffusion of hydrogen in olivine: Implications for water in the mantle. J Geophys Res 95:5079–5088
Mackwell SJ, Kohlstedt DL, Paterson MS (1985) The role of water in the deformation of olivine single crystals. J Geophys Res 90:11319–11333
Matsyuk SS, Langer K (2004) Hydroxyl in olivines from mantle xenoliths in kimberlites of the Siberian Platform. Contrib Mineral Petrol 147:413–437

Matsyuk SS, Langer K, Hösch A (1998) Hydroxyl defects in garnets in garnets from mantle xenoliths in kimberlites of the Siberian platform. Contrib Mineral Petrol 132:163–179

Matveev S, O'Neill HSTC, Ballhaus C, Taylor WR, Green DH (2001) Effect of silica activity on OH^- IR spectra of olivine: Implications for low-aSiO_2 mantle metasomatism. J Petrol 42:721–729

Matveev S, Portnyagin M, Ballhaus C, Brooker RA, Geiger CA (2005) FTIR spectrum of phenocryst olivine as an indicator of silica saturation in magmas. J Petrol 46:603–614

McCammon C, Kopylova MG (2004) A redox profile of the Slav mantle and oxygen fugacity control in the cratonic mantle. Contrib Mineral Petrol 148:55–68

Mei S, Kohlstedt DL (2000a) Influence of water on plastic deformation of olivine aggregates 1. Diffusion creep regime. J Geophys Res 105:21457–21469

Mei S, Kohlstedt DL (2000b) Influence of water on plastic deformation of olivine aggregates 2. Dislocation creep regime. J Geophys Res 105:21471–21481

Mierdel K, Keppler H (2004) The temperature dependence of water solubility in enstatite. Contrib Mineral Petrol 148:305–311

Miller GH, Rossman GR, Harlow GE (1987) The natural occurrence of hydroxide in olivine. Phys Chem Miner 14:461–472

Mosenfelder JL, Deligne NI, Asimow PD, Rossman GR (2006a) Hydrogen incorporation in olivine from 2–12 GPa. Am Mineral 91:285–294

Mosenfelder JL, Sharp TG, Asimow PD, Rossman GR (2006b) Hydrogen incorporation in natural mantle olivines, water in the mantle. American Geophysical Union, Washington

Nimis P, Taylor WR (2000) Single pyroxene thermobarometry for garnet peridotites. Part 1. Calibration and testing of Cr in Cpx barometer and an enststite-in-cpx thermometer. Contrib Mineral Petrol 139:541–554

Paterson MS (1982) The determination of hydroxyl by infrared absorption in quartz, silicate glasses and similar materials. Bull Minéral 105:20–29

Peslier AH, Luhr JF (2006) Hydrogen loss from olivines in mantle xenoliths from Simcoe (USA) and Mexico: Mafic alkalic magma ascent rates and water budget of the sub-continental lithosphere. Earth Planet Sci Lett 242:302–319

Peslier AH, Luhr JF, Post J (2002) Low water contents in pyroxenes from spinel-peridotites of the oxidized, sub-arc mantle wedge. Earth Planet Sci Lett 201:69–86

Rauch M, Keppler H (2002) Water solubility in orthopyroxene. Contrib Mineral Petrol 143:525–536

Ruedas T (2006) Dynamics, crustal thicknesses, seismic anomalies, and electrical conductivities in dry and hydrous ridge-centred plumes. Phys Earth Planet Inter 155:16–41

Skogby H, Rossman GR (1989) OH^- in pyroxene: an experimental study of incorporation mechanisms and stability. Am Mineral 74:1059–1069

Skogby H, Bell DR, Rossman GR (1990) Hydroxide in pyroxene: variations in the natural environment. Am Mineral 75:764–774

Sobolev NV, Lavent'ev YG, Pokhilenko NP, Usova LV (1973) Chrome-rich garnets from the kimberlites of yakutia and their parageneses. Contrib Mineral Petrol 40:39–52

Stalder R (2004) Influence of Fe, Cr and Al on hydrogen incorporation in orthopyroxene. Eur J Mineral 16:703–711

Stalder R, Behrens H (2006) D/H exchange in pure and Cr-doped enstatite: implications for hydrogen diffusivity. Phys Chem Miner 33:601–611

Stalder R, Skogby H (2002) Hydrogen incorporation in enstatite. Eur J Mineral 14:1139–1144

Stalder R, Skogby H (2003) Hydrogen diffusion in natural and synthetic orthopyroxene. Phys Chem Miner 30:12–19

Stalder R, Klemme S, Ludwig T, Skogby H (2005) Water incorporation in orthopyroxene: interaction of different trivalent cations. Contrib Mineral Petrol 150:473–485

Utada H, Koyama T, Shimizu H, Chave AD (2003) A semi-global reference model for electrical conductivity in the mid-mantle beneath the north Pacific region. Geophys Res Lett 30:1194. doi:10.1029/2002GL016092

Wang L, Zhang Y, Essene E (1996) Diffusion of the hydrous component in pyrope. Am Mineral 81:706–718

Wood BJ (1995) The effect of H_2O on the 410-kilometer seismic discontinuity. Science 268:74–76

Wood BJ, Virgo D (1989) Upper mantle oxidation state: ferric iron contents of lherzolite spinels by ^{57}Fe Mossbauer spectroscopy and resultant oxygen fugacites. Geochim Cosmochim Acta 53:1277–1291

Wood BJ, Pawley A, Frost DR (1996) Water and carbon in the Earth's mantle. Philos Trans R Soc Lond 354:1495–1511

Woodland AB, Koch M (2003) Variation in oxygen fugacity with depth in the upper mantle beneath the Kaapvaal craton, Southern Africa. Earth Planet Sci Lett 214:295–310

Zhao Y-H, Ginsberg SB, Kohlstedt DL (2004) Solubility of hydrogen in olivine: dependence on temperature and iron content. Contrib Mineral Petrol 23:1–10